Chinese Chemical Letters 34 (2023) 107662

Contents lists available at ScienceDirect

Chinese Chemical Letters

journal homepage: www.elsevier.com/locate/cclet

# Peptide-assembled siRNA nanomicelles confine $MnO_x$-loaded silicages for synergistic chemical and gene-regulated cancer therapy

Jingjing Li, Juanjuan Wei, Yixuan Gao, Qi Zhao, Jianghui Sun, Jin Ouyang, Na Na*

*Key Laboratory of Radiopharmaceuticals, Ministry of Education, College of Chemistry, Beijing Normal University, Beijing 100085, China*

ARTICLE INFO

*Article history:*
Received 30 March 2022
Revised 16 June 2022
Accepted 6 July 2022
Available online 8 July 2022

*Keywords:*
Peptide-assembled siRNA nanomicelles
$MnO_x$-loaded silicages
GSH-stimulated release
Mitochondria-targeted delivery
Cancer therapy

ABSTRACT

Chemodynamic therapy (CDT) is a promising therapeutic approach for *in situ* cancer treatment, but it is still hindered by inefficient single-modality treatment and the weak targeted delivery of reagents into mitochondria (the main site of intracellular ROS production). Herein, to obtain a multimodal strategy, peptide-assembled siRNA nanomicelles were prepared to confine ultrasmall $MnO_x$ in small silica cages (silicages), which is convenient for synergistic chemical and gene-regulated cancer therapy. Given the free energy and versatility of small silicages, as well as the excellent Fenton-like activity of ultrasmall $MnO_x$, $MnO_x$-inside-loaded silicages (10 nm) were prepared for CDT delivery to mitochondria. Subsequently, to obtain a synergistic CDT and gene silencing treatment, the peptide-mediated assembly of siRNA and $MnO_x$-loaded silicages were employed to obtain silicage@$MnO_x$-siRNA nanomicelles (SMS NMs). After multiple modifications, sequential cancer cell-targeted delivery, GSH-controlled reagent release of siRNA and mitochondria-targeted delivery of $MnO_x$-loaded silicages were successfully achieved. Finally, by both *in vitro* and *in vivo* experiments, SMS NMs were confirmed to be effective for synergistic chemical and gene-regulated cancer therapy. Our findings expand the applications of silicages and initiate the development of multimodal CDT.



Cancer cells have an altered mitochondrial redox state, with high levels of reactive oxygen species (ROS) and antioxidants (such as glutathione, GSH) [1–3]. This makes breaking the balance between ROS and antioxidants a potential approach for cancer treatment, triggering apoptotic cell death upon rapid ROS accumulation by antioxidant depletion [4–6]. For this reason, chemodynamic therapy (CDT), simply triggered by Fenton-active catalysts, is regarded as a promising therapeutic approach for *in situ* cancer treatment in response to highly selective endogenous stimulus [7–12]. In CDT, toxic $^{\bullet}OH$ is obtained *via* $H_2O_2$ reduction in the presence of Fenton-active low-valent transition metal ions, destroying redox homeostasis to induce cancer cell death [13–22]. To guarantee efficient intracellular production and avoid $^{\bullet}OH$ scavenging by intracellular GSH, metal-anchored nano agents were recently developed [23–30]. In addition, the co-encapsulation of different types of bioactive drugs also initiated the intracellular delivery *via* double emulsions [31]. However, the preparation and fabrication of double emulsions seem to be rather complex and unstable, reducing the drug efficacies. Hence, CDT is still hindered by the limited treatment effect from inefficient single-modality treatment and the loss and toxification of Fenton-active metal catalysts during delivery. Furthermore, the larger particles are difficult to enter the mitochondria for targeted CDT. Therefore, an alternative, low-toxicity, and multimodal CDT strategy is desirable for efficiently loading Fenton-active metal catalysts to target mitochondria.

Recently, ultrasmall (less than 10 nm) silica cages (silicages) were prepared *via* the self-assembly of silica structures by surfactant micelles [32]. With icosahedral symmetrical structures like viruses, silicage formation is associated with the energy minimizations, further endowing them with free energy for easy applications *via* electrostatic interactions [33]. Given the versatile surface chemistry for differentiable inner and outer surface modifications, silicage is an ideal CDT nanocarrier with regents hidden inside the cages. Meanwhile, to circumvent the complexity and enable spatial-temporal consistency of treatments, multimodal CDT providing gene silencing would be useful. However, a multimodal strategy of synergistic chemical and gene-regulated cancer therapy is still challenged by (1) the difficulties of unified loading of macromolecule gene-silencing reagents and inorganic metal species and (2) the difficulties of delivery of large complexed therapeutic drugs into mitochondria. Therefore, an alternative strategy for co-encapsulation of both silicage-loaded Fenton-active metal catalysts and gene silencing reagents could be ideal for effective multimodal CDT targeting mitochondria.

* Corresponding author.
*E-mail address:* nana@bnu.edu.cn (N. Na).

https://doi.org/10.1016/j.cclet.2022.07.005
1001-8417/

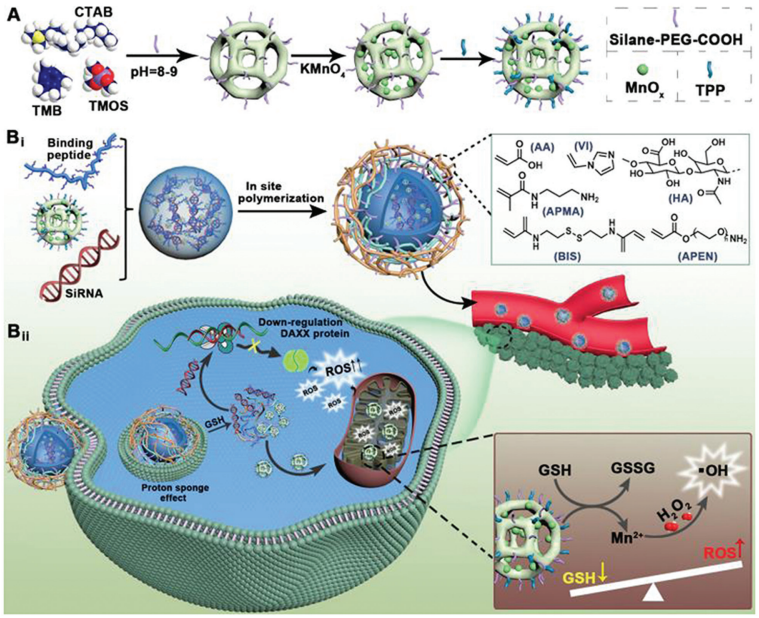


**Scheme 1.** Design of the siRNA-silicage nanomicelles and illustrations of the synergistic chemical and gene silencing treatment. (A) Preparation of $MnO_x$-functionalized silicage. (B) Construction of SMS NMs through peptide-mediated self-assembly (i) and the synergistic CDT process in cancer cells (ii). The inset is the GSH-initiated CDT with Fenton-active $MnO_x$ loaded inside the silicages in mitochondria.

Herein, to obtain a multimodal strategy, peptide-assembled siRNA nanomicelles were fabricated to confine $MnO_x$-loaded silicages (silicage@$MnO_x$-siRNA nanomicelles, SMS NMs) for synergistic chemical and gene silencing treatment. Given that DAXX-driven p62 phase condensation can promote p62 recruitment of Keap1 and Nrf2-mediated stress responses, siDAXX was selected to block DAXX to enhance CDT (*via* genetic disruption of intracellular redox homeostasis) [34]. Fenton-active ultrasmall $MnO_x$ was prepared and loaded inside the silicages, acting as CDT reagents in mitochondria. Inspired by tunability, porosity, and inclusiveness of nanomicelles, a peptide amphiphile-mediated self-assembly strategy was constructed to obtain consistent loading and co-encapsulation of siDAXX and ultrasmall $MnO_x$-functionalized silicages. Thereafter, the nanomicelles were modified with hyaluronic acid (HA) on GSH-cleavable polymers to target CD44-overexpressing tumor cells. This strategy enabled the efficient intracellular delivery of nanomicelles and the subsequent GSH-stimulated release of siDAXX and $MnO_x$-functionalized silicages for synergistic cancer therapy.

The siRNA-silicage nanomicelles were designed by the construction of $MnO_x$-inside loaded silicages followed by peptide-mediated self-assembly with siRNA, and the final polymerization coating outside the nanomicelles. Briefly, the silicages were prepared at pH 8-9, with cetyltrimethylammonium bromide (CTAB) as the surfactant micelle, tetramethyl orthosilicate (TMOS) as a sol-gel silica precursor, and hydrophobic mesitylene (TMB) to increase the size and deformability of the micelles (Scheme 1A). The obtained negatively charged silica clusters were attracted to the positively charged CTAB micelle surface, assembling into micelle-templated silicages.

Subsequently, multiple modifications were employed both inside and outside of the silicages to support the diversified functions. First, silane-PEG-COOH was added to further stabilize and functionalize the silicage with -COOH for the subsequent peptide-mediated self-assembly. Then, the inner surface of the silicages was functionalized with thiol using (3-mercaptopropyl) trimethoxy-silane (MTPMS), helping to achieve the loading of $MnO_x$ inner silicages. Possessing CDT-like catalytic properties, the loaded ultra-small $MnO_x$ would be well protected during the delivery, which would be more efficient for CDT. During the CDT, the $MnO_x$ can react with GSH to produce $Mn^{2+}$, which in turn converts $H_2O_2$ into $^{\bullet}OH$. In addition, the outer surface of the silicages was functionalized with -$NH_2$ using (3-aminopropyl)trimethoxy-silane (APTMS), which was further modified with (4-carboxybutyl)triphenylphosphonium bromide (TPP-COOH). Here, modified with -TPP, the SMS NMs were endowed with the ability to target mitochondria.

As shown in Scheme 1$B_i$, the SMS NMs were obtained through the peptide-mediated self-assembly of siRNA and silicages loaded with $MnO_x$-inside. The self-assembly was triggered by the interaction between positively charged peptides and negatively charged silicages. The peptides with valine residues were chosen to provide a hydrophobic core region to exclude the competitive adsorption between water molecules and hydrogen bond stacked silicages [35]. This induced homogenous self-assembly between the peptide and silicages. In addition, positive peptides (consisting of valine and lysine) were freely soluble, monomeric, and intrinsically disordered in water. Excess peptides also provide enough surface area to bind and fold the siRNA. These further ensured the production of nanomicelles by electrostatic assembly with negatively charged siRNA [36,37]. The co-encapsulation of Fenton reagent and siRNA can enhance oxidative stress and reduces antioxidant capacity of tumor cells. Therefore, this can resolve the contradiction between high oxidative stress and strong antioxidant capacity in tumor cells at the gene level.

Thereafter, a GSH-cleavable coating was constructed by polymerization outside the nanomicelles. The polymerization can protect the siRNA/peptides from proteolysis and denaturation while increasing their local accumulation at the cancer site. Given the heterogeneous charges within the nanomicelles, cationic-anionic monomers of *N*-(3-aminopropyl)methacrylamide hydrochloride (APMA) and acrylic acid (AA) were selected to package the nanomicelles through electrostatic interactions. Furthermore, monomer of 1-vinylimidazole(VI) was selected to ensure the proton sponge effect. Another monomer of -$NH_2$-conjugated acrylate poly(ethylene glycol) (APEN) was used to obtain positive charges, which can attract CD44-targeted hyaluronic acid (HA) *via* hydrogen bonding and van der Waals interactions. Finally, the *in situ* free-radical polymerization of the aforementioned monomers

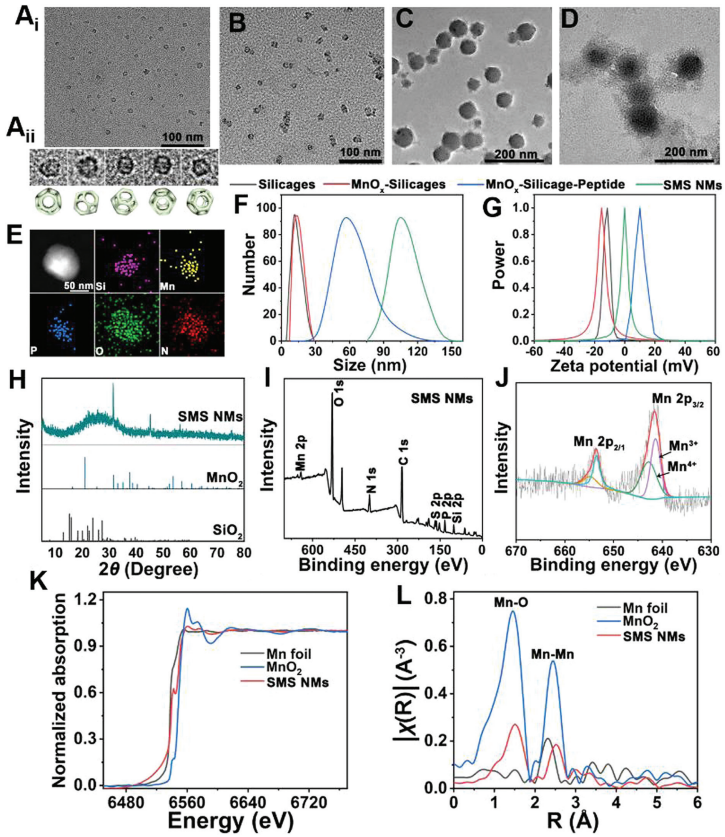


**Fig. 1.** Characterization of SMS NMs. (A) TEM images of silicages ($A_i$) and magnified images with models ($A_{ii}$). (B) With $MnO_x$ loaded inside silicages. (C) The nanomicelles of peptide-mediated self-assembly of siRNA with $MnO_x$-loaded silicages. (D) The final SMS NMs coated by the polymerizations. (E) HAADF-STEM image, (F) DLS, (G) Zeta potential, and (H) XRD patterns of SMS NMs, $MnO_2$ and $SiO_2$. (I) XPS spectra of SMS NMs. (J) Mn 2p XPS spectra of SMS NMs. (K) Mn K-edge XANES profiles and (L) EXAFS spectra of SMS NMs, $MnO_2$ and Mn foil.

was initiated in the presence of GSH-degradable crosslinker (BIS), ammonium persulfate and *N*,*N*,*N*′,*N*′-tetramethylethylenediamine (TMEDA). The outer PEG shell not only ensure the water-solubility of SMS NMs, but also provide flexibility to modify targeted molecules. Thereby, the SMS NMs were obtained for *in vivo* applications.

Scheme $1B_{ii}$ illustrates the process of sequential targeting of SMS NMs into cancer cells, then to the mitochondria, and subsequent synergistic chemical and gene silencing therapy. Targeting HA to CD44, SMS NMs were delivered into cancer cells, followed by VI-facilitated endosomal escape *via* the proton sponge effect. Thereafter, in the GSH-rich environments of the cancer cytosol, the polymer coating of SMS NMs was cleaved upon the response of BIS to GSH. Furthermore, the siRNA and $MnO_x$-loaded silicages were released into the intracellular environment for the synergistic treatments. Briefly, $MnO_x$-loaded silicages targeted the mitochondria under the guidance of TPP on silicage surface. This induced the Fenton-like CDT by $MnO_x$, which was facilitated by the consumption of GSH. Simultaneously, the gene silencing treatment was synergistically deployed by siRNA (siDAXX) to reduced DAXX levels.

To confirm the successful preparation of SMS NMs, morphology characterization was employed. As demonstrated by transmission electron microscopy (TEM), the silicages showed a diameter of approximately 9 nm (Fig. $1A_i$), and their silicage structure was confirmed by the magnified images (Fig. $1A_{ii}$). *Via* loading of $MnO_x$ into silicages, the diameter increased to approximately 10 nm (Fig. 1B). After the peptide-mediated self-assembly of siRNA and $MnO_x$-loaded silicages, the size of spherical nanomicelles reached to about 65 nm (Fig. 1C). After coverage by the polymerizations, the final size of SMS NMs was approximately 93 nm (Fig. 1D). The coverage by the polymerization was further confirmed by the high-angle annular dark-field scanning TEM (HAADF-STEM)-based elemental mapping (Fig. 1E).

The nanomicelles were then examined by dynamic light scattering (DLS) analysis, which was in accordance with the progressively increasing size during the step-by-step synthesis (Fig. 1F). The increased size was generated from the modifications on both inner and outer surfaces of silicages by $MnO_x$ and -TPP, respectively. In addition, the zeta potential of silicages (−11.56 mV) decreased to −15.37 mV after being loaded inside $MnO_x$. The zeta potential was 9.98 mV after the peptide-mediated self-assembly of siRNA with $MnO_x$-loaded silicages, which further decreased to −0.15 mV after the final polymerization (Fig. 1G). These results are consistent with the preparation procedures, confirming the successful synthesis of SMS NMs.

Subsequently, the chemical compositions of the SMS NMs were investigated by X-ray diffraction (XRD) and X-ray photoelectron spectroscopy (XPS) techniques. The characteristic peaks of both $SiO_2$ and $MnO_2$ in XRD demonstrated the successful coating of $MnO_x$ inner the silicages (Fig. 1H). XPS spectra showed the presence of Si, P, S, Mn, and O (Fig. 1I), also confirming the successful preparation of SMS NMs. Furthermore, characteristic peaks at 654.2 and 642.4 eV were assigned to Mn $2p_{1/2}$ and Mn $2p_{3/2}$ peaks, whose binding energies were consistent with valent values of Mn in $MnO_2$ (Fig. 1J). In addition, X-ray absorption near-edge structure (XANES) and extended X-ray absorption fine structure (EXAFS) measurements were performed to study the electronic structure and coordination environment of the Mn species in SMS NMs. Fig. 1K indicates the oxidation state of Mn ($Mn^{\delta+}$, $0 < d < 4$),

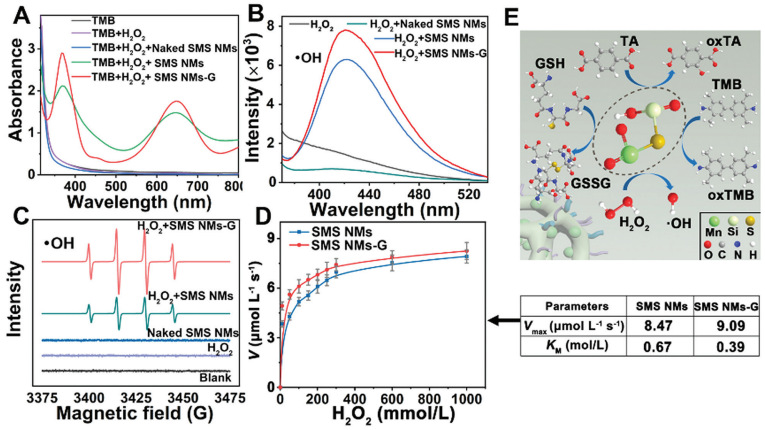


**Fig. 2.** (A) UV-vis spectra of TMB solution after reaction with different species for 30 min. (B) Generation of •OH as indicated by the enhanced fluorescence of TA. (C) ESR spectra of different groups for the detection of •OH. (D) Enzyme kinetics of SMS NMs. (E) Schematic illustration of CDT.

whose absorption edge is between those of $MnO_2$ and Mn foil. The R-space spectrum of EXAFS exhibits a main peak of Mn-O at 1.50 Å and Mn-Mn scattering peak at 2.5 Å (Fig. 1L), further demonstrating the successful synthesis of $MnO_2$. In addition, UV-vis absorption spectroscopy also confirmed the successful modification of silicages with $MnO_2$ and TPP (Fig. S1 in Supporting information).

To explore the CDT behavior of the SMS NMs, the catalase (CAT)-like activity was examined, which generates hydroxyl radicals (•OH) by reducing $H_2O_2$. First, the CAT-like activity was investigated by monitoring the absorption changes of 3,3,5,5'-tetramethylbenzidine (TMB) at 652 nm. As illustrated (Fig. 2A), no apparent change was detected without SMS NMs, while a significant increase in TMB absorbance was observed when TMB was incubated with $H_2O_2$ and SMS NMs. Significantly, the TMB absorption further increased after GSH treatment, which was ascribed to the GSH-stimulated release of Fenton-like $Mn^{2+}$ to promote CDT efficiency.

In addition, •OH was demonstrated to be generated by the significantly enhanced fluorescence of terephthalic acid (TA) (Fig. 2B). To directly identify ROS, electron spin resonance (ESR) spectra were collected to demonstrate the presence of •OH using 5,5-dimethyl-1-pyrroline *N*-oxide (DMPO) as a trapping probe. SMS NMs induced the generation of a four-line spectrum with a relative intensity of 1:2:2:1, which is the characteristic spectrum of DMPO/•OH (Fig. 2C). Furthermore, a prominent •OH signal was also exhibited, indicating enhanced Fenton catalytic activity by GSH-treated SMS NMs. Moreover, the typical Michaelis-Menten kinetics for mimicking CAT activity were examined using $H_2O_2$ as the substrate. As indicated by $K_M$ and $V_{max}$ in Fig. 2D, the present SMS NMs exhibited an improved enzymatic reaction with GSH treatment.

Therefore, •OH was confirmed to be generated to facilitate CDT by SMS NMs. As shown in Fig. 2E, upon the stimulation of relatively high expression of GSH in cancer cells, the released $MnO_x$ from the silicages was reduced to $Mn^{2+}$ by reductive GSH. Simultaneously, GSH was oxidized into GSSG. Thereafter, the Fenton-active $Mn^{2+}$ facilitated the generation of •OH in the presence of overexpressed $H_2O_2$ in cancer cells. In fact, the catalytic activity of $MnO_x$ in silicages can be successfully exhibited by the enhanced fluorescence of TA and the absorption changes of TMB under oxidation.

To evaluate the sequential targeted delivery, controlled reagent release, as well as synergistic chemical and gene silencing treatment, intracellular examination was employed. With HeLa cells as models, cell imaging of step-by-step procedures was carried out using confocal laser scanning microscopy (CLSM). To investigate the tumor cell-targeted delivery, siRNA was labeled with Cy5 for cell imaging. First, the efficient cellular uptake of SMS NMs by CD44-overexpressing HeLa cells was confirmed by the comparison of SMS NMs with and without HA-modification (Fig. S2 in Supporting information). SMS NMs escaped from the endosome due to the proton sponge effect by imidazole groups. Subsequently, SMS NMs were cleaved to release siRNA and $MnO_x$-loaded silicages in response to GSH.

The released silicages targeted the mitochondria, which was confirmed by cell imaging with red MitoTracker dye (to indicate the mitochondria location). The silicages were labelled with green FAM for tracking. As demonstrated by the red and green channels, intramitochondrial accumulation of the silicages was confirmed (Fig. 3A). This mitochondria-targeted delivery was attributed to molecular recognition by TPP, owing to electrostatic and lipophilic attractions with mitochondrial membrane. This facilitated the subsequent mitochondrial-responsive ROS (•OH) generation for CDT. To indicate the generation of intracellular ROS, the DCFH-DA probe was selected to generate fluorescent DCFH from the rapid oxidation by ROS. As shown in Fig. 3B, the strongest fluorescence was exhibited with SMS NMs treatment. This demonstrated synergically enhanced ROS generation in the presence of siRNA and $MnO_x$-loaded silicages. Therefore, the stress responses of DAXX silencing and Fenton-active CDT were synergically employed. These results were in accordance with the results from flow cytometry analysis (Fig. S4 in Supporting information).

The treatment effects of the synergistic chemical and gene silencing were confirmed by the cytotoxicity to HeLa cells treated with different NM species (Fig. 3C). In addition, the mitochondrial membrane potential ($\Delta\Psi_m$) of HeLa cells was detected by a JC-1 kit, whose fluorescent signal changed from red to green in apoptotic cells with a lower $\Delta\Psi_m$ [38]. After treatment with SMS NMs (Fig. 3D), the highest green fluorescence but no obvious red signal was recorded, confirming its more severe mitochondrial membrane disruption by synergistic treatments. This result also corresponded to the calcein acetoxymethyl ester (calcein AM)/propidium iodide (PI) detection and the quantitative Annexin V-FITC/PI assay. As shown in Fig. 3E, without any treatment, cells lived to give significant green emissions (stained by calcein AM). After SMS NMs treated, all cells generally died to exhibit only red signals (stained by PI). Furthermore, the *in vitro* synergistic performance was extensively evaluated using the dual fluorescence of Annexin V-FITC/PI through flow cytometry. As shown in Fig. 3F, after treatment with siRNA or $MnO_x$-loaded silicages, 39.58% and 70.19% apoptosis percentages were observed. The highest percentage at 80.41% was obtained for the synergistic treatment by SMS NMs.

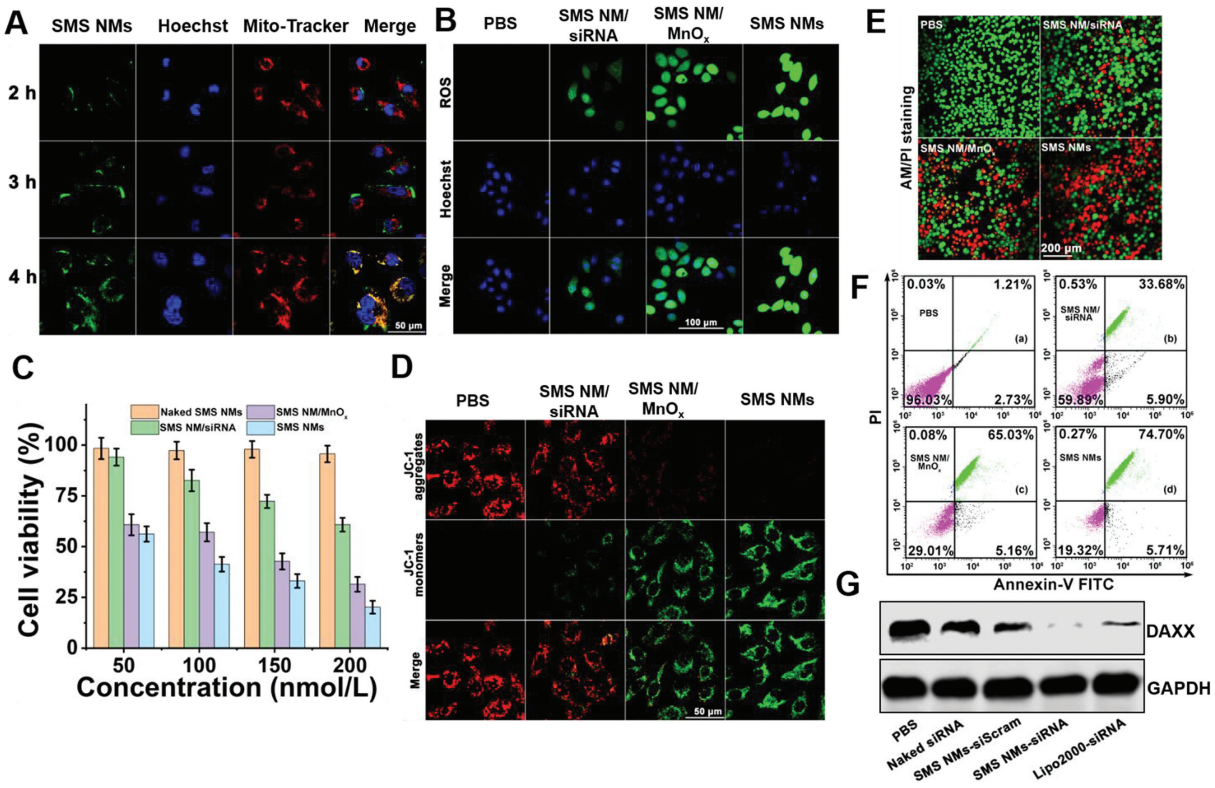


**Fig. 3.** Intracellular exploration of the developed SMS NMs. (A) CLSM images of HeLa cells pretreated with MitoTracker, followed by incubation with SMS NMs for different times. (Blue: Hoechst; green: SMS NMs; Red: MitoTracker). (B) CLSM monitoring of ROS generation after incubation with different SMS NM species. (C) Cell viability of HeLa cells treated with various concentrations of naked SMS NMs, SMS NM/siRNA, SMS NM/$MnO_x$, or SMS NMs (from 50 nmol/L to 200 nmol/L). (D) Fluorescence imaging to evaluate changes of mitochondrial membrane potential. (E) Calcein-AM/PI staining images of HeLa cells after incubation with PBS (blank), SMS NM/siRNA, SMS NM/$MnO_x$ and SMS NMs. (F) Flow cytometric analysis of apoptosic cells after different treatments: PBS (blank), SMS NM/siRNA, SMS NM/$MnO_x$, and SMS NMs. (G) Western blot analysis of DAXX protein in HeLa cells after different treatments (For interpretation of the references to color in this figure, the reader is referred to the web version of this article.).

Furthermore, the gene silencing of SMS NMs was also examined with a green fluorescent protein (GFP)-containing gene as the silencing target in a HeLa-GFP cell line. The significant silencing efficiency was demonstrated by cell imaging and flow cytometry, with ~80% decrease in the fluorescent signal. This was more significant than naked siRNA treatment (Fig. S3 in Supporting information). To evaluate the gene silencing effect, the oxidative stress-associated gene DAXX in cancer cells treated with SMS NMs was examined by Western blot. The best gene silencing therapeutic efficiency occurred after treatment with SMS NMs (Fig. 3G), which was even more effective than the traditional Lipo 2000 delivery of siRNA. Therefore, synergistic chemical and gene silencing treatments were confirmed.

Finally, the *in vivo* application of the SMS NMs was employed. The therapeutic effect of SMS NMs in HeLa xenograft-tumor-bearing mice was evaluated *via* intravenous injection. The SMS NMs without target groups (Control SMS NMs), SMS NMs modified with TPP (SMS-TPP NMs) and those modified with TPP and HA (SMS-TPP-HA NMs) were injected for comparisons. The strongest fluorescence signals were observed in the tumor region treated with SMS-TPP-HA NMs (Fig. 4A), confirming their remarkable tumor-targeting abilities. This result matches the *ex vivo* imaging of major organs and tumors from the mice (Figs. 4B and C, and Fig. S5 in Supporting information).

Subsequently, the antitumor effects of SMS NMs were further evaluated in HeLa xenograft tumor-bearing mice *in vivo*. After the tumor volume reached 100–120 $mm^3$, the nude mice were randomly divided into five groups (3 mice per group), treated with PBS, naked SMS NMs, SMS NM/siRNA, SMS NM/$MnO_x$, or the present SMS NMs. As shown in Figs. 4D and E, the strongest inhibition on growth of tumors was recorded after treatment with SMS NMs. Notably, no significant change in the mice weight was recorded, demonstrating good biocompatibility (Fig. 4F). Besides, histopathological examination (H&E) also confirmed the synergistic therapy (Fig. 4G), showing the most prominent damage in the tumor tissue with SMS NMs treatment. Furthermore, no obvious inflammation or disorganization was observed in the major organs (including heart, liver, spleen, lung, and kidney) of each treatment group after 31 days (Fig. S6 in Supporting information). Therefore, along with good biocompatibility, the developed SMS NMs exhibited ideal therapeutic efficiency.

In conclusion, peptide-assembled siRNA nanomicelles were fabricated to confine $MnO_x$-loaded silicages, which were convenient for synergistic chemical and gene silencing treatment of cancer cells. Given the free energy and versatility of ultrasmall silicages, Fenton-active $MnO_x$ was loaded inside the silicages for efficient CDT. To obtain consistent loading of macromolecule gene-silencing reagents and inorganic species in the $MnO_x$-loaded silicages, a peptide amphiphile-mediated self-assembly strategy was constructed. Therefore, sequential cancer cell-targeted delivery, GSH-controlled reagent release of siRNA and mitochondria-targeted delivery of CDT reagents were successfully applied for synergistic chemical and gene silencing. The siRNA downregulated the expression of antioxidant enzymes, which enhanced CDT-mediated oxidative stress to suppress tumor progression. This multimodal treatment integrates the advantages of two treatment methods into one nanomicelle and achieve a synergistic superadditive $(1+1 > 2)$ therapeutic effect. This work not only successfully achieved a multimodal CDT strategy, but also expanded the application of ultrasmall silicages in the field of clinical therapy. Inspired by the de-

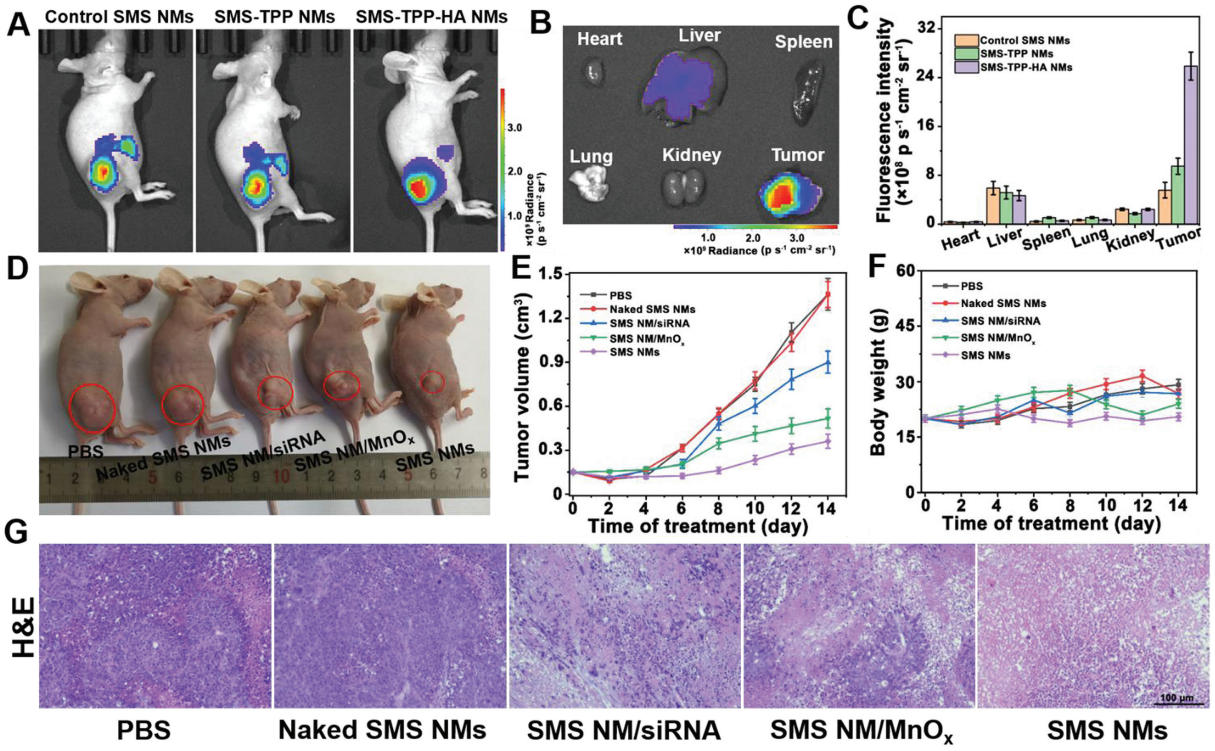


**Fig. 4.** *In vivo* explorations of the tumor-specific accumulation and therapeutic performance of SMS NMs in HeLa tumor-bearing mice. (A) Biodistribution of control SMS NMs, SMS-TPP NMs, and SMS-TPP-HA NMs in HeLa tumor-bearing nude mice after 8 h of intravenous injection. (B) *Ex vivo* fluorescence imaging of the main organs and tumor tissues. (C) Average fluorescent signals of the main organs and tumors. (D) Pictures of tumor volume changes after 14 days of treatment. (E) Time-dependent tumor-growth and (F) body weight evolution curves of mice with different treatments. (G) H&E staining of tumor tissues after different treatments.

sign and application of this platform, engineering of other nanomicelles could also be implemented for wider biological applications.

## Declaration of competing interest

The authors declare that they have no known competing financial interests or personal relationships that could have appeared to influence the work reported in this paper.

## Acknowledgments

N. Na, J. Li, J. Wei, Y. Gao, Q. Zhao and J. Sun gratefully acknowledge the financial support provided by the National Natural Science Foundation of China (NNSFC, No. 21874012) and the National Key Research and Development Program of China (No. 2019YFC1805600). J. Ouyang is grateful for the financial support provided by NNSFC (No. 21974010).

## Supplementary materials

Supplementary material associated with this article can be found, in the online version, at doi:10.1016/j.cclet.2022.07.005.

## References

[1] S.E. Weinberg, N.S. Chandel, Nat. Chem. Biol. 11 (2015) 9–15.
[2] L.A. Sena, N.S. Chandel, Mol. Cell 48 (2012) 158–167.
[3] G.S. Shadel, T.L. Horvath, Cell 163 (2015) 560–569.
[4] P.H.G.M. Willems, R. Rossignol, C.E.J. Dieteren, M.P. Murphy, W.J.H. Koopman, Cell Metab. 22 (2015) 207–218.
[5] S.S. Sabharwal, P.T. Schumacker, Nat. Rev. Cancer 14 (2014) 709–721.
[6] B.C. Dickinson, C.J. Chang, Nat. Chem. Biol. 7 (2011) 504–511.
[7] F. Jiang, C. Yang, B. Ding, et al., Chin. Chem. Lett. 33 (2022) 2959–2964.
[8] N. Gong, X. Ma, X. Ye, et al., Nat. Nanotechnol. 14 (2019) 379–387.
[9] X. Hu, F. Li, F. Xia, et al., J. Am. Chem. Soc. 142 (2020) 1636–1644.
[10] B. Ma, S. Wang, F. Liu, et al., J. Am. Chem. Soc. 141 (2019) 849–857.
[11] S. Wang, G. Yu, Z. Wang, et al., Angew. Chem. Int. Ed. 58 (2019) 14758–14763.
[12] X. Li, R. Luo, X. Liang, Q. Wu, C. Gong, Chin. Chem. Lett. 33 (2022) 2213–2230.
[13] Y. Liu, X. Ji, W.W.L. Tong, et al., Angew. Chem. Int. Ed. 57 (2018) 1510–1513.
[14] M. Ye, Y. Gao, M. Liang, et al., Chin. Chem. Lett. 33 (2022) 4197–4202.
[15] Z. Dong, L. Feng, Y. Chao, et al., Nano Lett. 19 (2019) 805–815.
[16] N. Chen, W. Fu, J. Zhou, et al., Chin. Chem. Lett. 32 (2021) 2405–2410.
[17] L.S. Lin, J. Song, L. Song, et al., Angew. Chem. Int. Ed. 57 (2018) 4902–4906.
[18] Y. Wang, C. Zhang, H. Zhang, L. Feng, L. Liu, Chin. Chem. Lett. 33 (2022) 4605–4609.
[19] W. Xuan, Y. Xia, T. Li, et al., J. Am. Chem. Soc. 142 (2020) 937–944.
[20] Z. Cao, L. Zhang, K. Liang, et al., Adv. Sci. 5 (2018) 1801155.
[21] C. Liu, D. Wang, S. Zhang, et al., ACS Nano 13 (2019) 4267–4277.
[22] P. Yu, X. Li, G. Cheng, et al., Chin. Chem. Lett. 32 (2021) 2127–2138.
[23] L. Lin, S. Wang, H. Deng, et al., J. Am. Chem. Soc. 142 (2020) 15320–15330.
[24] L. Shi, Y. Wang, C. Zhang, et al., Angew. Chem. Int. Ed. 60 (2021) 9562–9572.
[25] X. Chen, Y. Chen, C. Wang, et al., Angew. Chem. Int. Ed. 60 (2021) 21905–21910.
[26] C. Liu, Y. Cao, Y. Cheng, et al., Nat. Commun. 11 (2020) 1735.
[27] W. Zhen, Y. Liu, W. Wang, et al., Angew. Chem. Int. Ed. 59 (2020) 9491–9497.
[28] X. Zhao, K. Guo, K. Zhang, et al., Adv. Mater. 34 (2022) 2108263.
[29] Y. Wang, Y. Li, Z. Zhang, et al., Adv. Mater. 33 (2021) 2103748.
[30] Y. Wang, Y. Song, G. Zhu, D. Zhang, X. Liu, Chin. Chem. Lett. 29 (2018) 1685–1688.
[31] N.P. Aditya, S. Aditya, H. Yang, et al., Food Chem. 173 (2015) 7–13.
[32] K. Ma, Y. Gong, T. Aubert, et al., Nature 558 (2018) 577–580.
[33] R. Zandi, D. Reguera, R.F. Bruinsma, W.M. Gelbart, J. Rudnick, Proc. Natl. Acad. Sci. U. S. A. 101 (2004) 15556.
[34] Y. Yang, T.L. Willis, R.W. Button, et al., Nat. Commun. 10 (2019) 3759.
[35] S.V. Patwardhan, F.S. Emami, R.J. Berry, et al., J. Am. Chem. Soc. 134 (2012) 6244–6256.
[36] K. Nagy-Smith, E. Moore, J. Schneider, R. Tycko, Proc. Natl. Acad. Sci. U. S. A. 112 (2015) 9816.
[37] S. Guan, A. Munder, S. Hedtfeld, et al., Nat. Nanotechnol. 14 (2019) 287–297.
[38] J. Sun, X. Cai, C. Wang, et al., J. Am. Chem. Soc. 143 (2021) 868–878.